Major mineral fraction and physical properties of carbonated peridotite (listvenite) from ICDP Oman Drilling Project Hole BT1B inferred from X-ray CT core images

Keishi Okazaki[1*], Katsuyoshi Michibayashi[2], Kohei Hatakeyama[3], Natsue Abe[4,5], Kevin T.M. Johnson[6,7], Peter B. Kelemen[8], and the Oman Drilling Project Phase I Science Team

[1]Kochi Institute for Core Sample Research, Japan Agency for Marine-Earth Science and Technology (X-star, JAMSTEC), Kochi 783-8502, Japan

[2] Department of Earth and Planetary Sciences, Graduate School of Environmental Studies, Nagoya University, Nagoya 464-8601, Japan

[3]Department of Earth and Planetary Systems Science, Hiroshima University, Hiroshima 739-8526, Japan

[4]Mantle Drilling Promotion Office, Japan Agency for Marine-Earth Science and Technology (MarE3, JAMSTEC), Kanagawa 236-0001, Japan

[5]Division of Natural System, Graduate School of Natural Science & Technology, Kanazawa University, Kanazawa 920-1192, Japan

[6] Department of Geology and Geophysics, University of Hawai‘i at Mānoa, Hawaii 96822, USA

[7]Marine Geology and Geophysics Division of Ocean Sciences, National Science Foundation, Virginia 22314, USA

[8]Lamont Doherty Earth Observatory, Columbia University, New York 10964, USA

*Corresponding author: Keishi Okazaki (JAMSTEC)

E-mail: okazakik@jamstec.go.jp; Tel: +81-88-878-2244; Fax: +81-88-878-21924

Key points (Max. 140 characters):

1. A method was developed to determine the downhole mineral fractions of drill cores

from continuous X-ray CT images.

2. Quartz–magnesite–dolomite fractions were estimated from X-ray CT images of listvenite cores from ICDP Oman Drilling Project Hole BT1B.
3. Results indicate limited material transfer during carbonation and hydration of the Oman Ophiolite, except for Si, Ca, CO_2, and H_2O.

Keywords: Ophiolite, Listvenite, X-ray CT, Carbonation, Mantle, Oceanic plate, Carbon storage

Abstract (247/250 words)

We evaluated the mineral fractions of listvenite (completely carbonated peridotite) in Hole BT1B drilled by the ICDP Oman Drilling Project from 3D X-ray Computed Tomography (XCT) images. Total >250,000 XCT images from continuous ~200 m listvenite core samples were analyzed. Histograms of the intensity of X-ray attenuation (XCT number) of each XCT core-slice image were fitted assuming that the CT histogram is composed of magnesite, quartz, and dolomite peaks. These mineral peaks were confirmed by comparison of XCT numbers with chemical mapping data obtained using an XRF core scanner. In most core sections, XCT data indicate that listvenite matrix is composed of magnesite and quartz, consistent with discrete XRD and XRF data. Veins are composed mostly of dolomite. The mean abundance of dolomite in listvenite from BT1B is 11 vol.%, whereas that in core sections within 15 m of the basal thrust is >50 vol.%, suggesting that the basal thrust acted as a pathway for Ca- and CO_2-rich fluids. The overall SiO_2:MgO:CaO ratio in BT1B is 43:51:5, similar to that of onboard XRF data (41:54:5) whereas lower SiO_2 fraction than that of Oman peridotite (39:60:1), indicating enrichment of Si during carbonation. P- and S-wave velocities and density of listvenite is close to that of peridotite while higher than that of serpentinites. These results suggest that limited material transfer during carbonation and hydration of the Oman Ophiolite, except for Si, Ca, CO_2 and H_2O, but potential as an overlooked carrier of CO_2 into the deep of Earth's interior.

1. Introduction

To understand planetary-scale fluid circulation from the surface to deep regions of Earth, it is important to constrain how fluids are captured/released by hydration/dehydration and carbonation/decarbonation of minerals and the associated volumes of these fluids. Moreover, the distribution of earthquakes and island arc volcanism can be influenced by the distribution of volatiles (cf. Abers et al. (2013); Mibe et al. (1999); Okazaki and Hirth (2016); Omori et al. (2004)). Hydrated/carbonated lithospheric mantle materials (i.e., ultramafic rocks) could be the primary carrier of volatiles into deep regions of Earth, as their volumes are larger than those of subducting sediments and oceanic crust (i.e., felsic and mafic rocks). Seismic observations suggest the presence of fluids at the corner of the mantle wedge (Kamiya & Kobayashi, 2000; Nakajima & Uchida, 2018) as well as in subducting slabs (Audet et al., 2009; Peacock et al., 2011; Tsuji et al., 2008). However, as the evaluation of the alteration intensity of the mantle lithosphere from the velocity structure is totally model dependent, and there has been no direct drilling into the mantle, quantitative estimation of the intensity of alteration of the lithospheric mantle is lacking.

Ophiolites, which are fossil material of paleo-oceanic plates, are obducted and widely exhumed on Earth's surface (Dilek & Furnes, 2011). The Samail Ophiolite (Oman Ophiolite, hereafter), which is located in the Sultanate of Oman and the United Arab Emirates, is the most extensive and best-exposed cross-section of oceanic lithosphere from sediments and pillow lavas to mantle harzburgite (Figure S1). The basal thrust at the base of the ophiolite separates the ophiolite sequence from the underlying metamorphic sole consisting of greenschist- to amphibolite-facies metasediments and metabasalts. The metamorphic sole is underlain by Permian to Late Cretaceous

formations composed mainly of marine sediments, meta-volcanic rocks, and limestone (Hacker & Mosenfelder, 1996; Ishikawa et al., 2005). Overall, peridotite in the Oman Ophiolite has undergone a degree of hydration (serpentinization), probably during obduction. In addition to the serpentinization, some parts of the peridotite close to the basal thrust are carbonated. Listvenite, which is fully carbonated mantle material, was originally defined as quartz–carbonate metasomatic rocks that were initially regarded in terms of their relationship to gold mineralization and other ore deposits, but more recently has been highlighted as a natural analog to mineral carbon storage (Beinlich et al., 2020; Falk & Kelemen, 2015; Hansen et al., 2005; Kelemen et al., 2011; Streit et al., 2012). It is considered that the basal thrust of the Oman Ophiolite was active as the paleo plate boundary between the ophiolite body and over-thrusted oceanic plate and as a pathway for fluids since the initial stage of obduction (Hacker & Mosenfelder, 1996; Ishikawa et al., 2005). Since the late stage of obduction, carbonation of obducted peridotites and serpentinites has been occurring continuously close to the basal thrust (Falk & Kelemen, 2015). The deformation structure and lithological and geochemical properties of these rocks have been closely investigated by recent studies (Beinlich et al., 2020; Falk & Kelemen, 2015; Menzel et al., 2020).

In the present study, we developed a method to estimate the mineral fraction of core samples from X-ray computed tomography core images with confirmation using chemical mapping data from an X-ray fluorescence (XRF) core scanner. The technique of non-destructive X-ray computed tomography is widely used, not only for medical purposes but also for industrial and material science applications requiring acquisition of internal structures of objects. Similarly, in earth sciences, this method has been applied, for example, to evaluate the grades of ore deposits, analyze samples from asteroid bodies,

and observe the real-time development of microstructures during deformation (Baker et al., 2012; Godel, 2013; Ketcham & Carlson, 2001; Kyle & Ketcham, 2015; McBeck et al., 2019; Okumura et al., 2008; Renard et al., 2016; Tsuchiyama et al., 2011). Using this technique, we estimated continuous downhole-scale major mineral and element fractions of listvenite in Hole BT1B drilled by the ICDP Oman Drilling Project (Kelemen et al., 2020b). These results were compared with physical property and geochemical data of individual discrete listvenite samples from BT1B analyzed onboard D/V *Chikyu* in 2017 (Kelemen et al., 2020b, 2020c), on which basis we infer material transfer by CO_2-rich fluids during carbonation and potential as an overlooked carrier of CO_2 into the deep of Earth's interior.

2. Core sample and method

2.1. Listvenite core from ICDP Oman Drilling Project Hole BT1B

Continuous drilling from the bottom of the ophiolite through the basal thrust to the footwall metamorphic sole was conducted in Hole BT1B by the ICDP Oman Drilling Project (Figure S1). Listvenite (completely carbonated former peridotite) is the main lithology in Hole BT1B and is also found in other ophiolite bodies. Figure 1 presents the downhole lithology of the core sample obtained from Hole BT1B. Listvenite is composed mainly of magnesite, quartz, dolomite, and Fe-hydroxide, with minor chromian spinel and chromian mica (fuchsite; (Kelemen et al., 2020c). Two serpentinite and ophicarbonate intervals also occur above the basal thrust. Below the basal thrust, metamorphic sole composed of greenschist/greenstone is the main lithology.

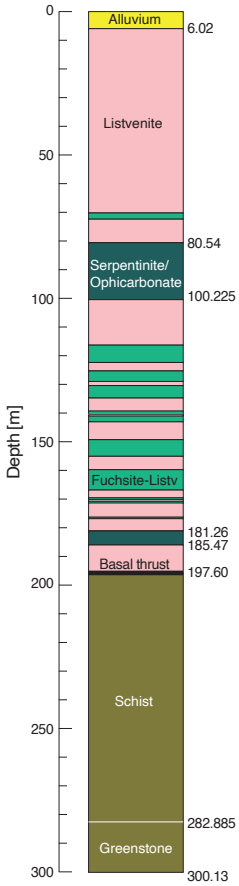

Figure 1. Principal lithologies of recovered core samples from Hole BT1B.

2.2. X-ray computed tomography core images taken onboard D/V *Chikyu*

All raw X-ray computed tomography (XCT) data used in this study are archived on the ICDP website and have already been published in the initial report on the ICDP Oman Drilling Project (Kelemen et al., 2020a, 2020b, 2020c). Therefore, in this and next sections, we briefly describe the methods and procedures for XCT and XRF core scanning.

All core samples obtained by the Oman Drilling Project have been passed through an XCT scanner, which enables the non-destructive observation of the internal structure of core samples and is a routine measurement of the IODP drilling performed by D/V *Chikyu*. The procedures for XCT scanning adopted in the present study followed those of previous IODP expeditions (e.g., IODP Expedition 322, Underwood et al. (2010); and IODP Expedition 343, Expedition 343/343T Scientists (2013)), which is based on the

previous studies (GE healthcare, 2013; Mees et al., 2003; Nakano et al., 2000) . A medical-use XCT scanner (Discovery CT 750HD, GE Medical Systems) was used for the measurements. The excitation voltage and current for the X-ray tube (X-ray source) were 140 kV and 100 mA, respectively. All core sections of BT1B were scanned by the XCT scanner with resolutions of 0.176 mm/pixel for the core-axis-normal (X and Y) directions and 0.625 mm/pixel for the core-axis-parallel (Z) direction. Listvenite core sections have similar dimensions (~63.5 mm in diameter) and thus similar volumes; therefore, the XCT number provides information regarding the physical and chemical properties of the core samples. More details on the XCT scanning procedure can be found in the initial report on the ICDP Oman Drilling Project (Kelemen et al., 2020a, 2020b, 2020c).

Figure 2a shows an image taken using multi-sensor core logger (MSCL-I) of the archive half split core surface of core section BT1B 49Z-1, and Figure 2b shows a 2D XCT image (X–Z slice) reconstructed from X–Y slice images of this core section. Examples of the X–Z images are presented in Figure 2c–h. The color indicates the CT number of each voxel, which is defined as;

$$CT\ number = [(\mu_t - \mu_w)/\mu_w] \times 1000 \quad (1)$$

where μ_t is the linear attenuation coefficient (LAC) of the target material (minerals and airs, in this study), and μ_w is the LAC for water. X-ray intensity varies as a function of X-ray path length and the linear attenuation coefficient (LAC) of the target material as;

$$I = I_0 \times e^{-\mu L} \quad (2)$$

where I is the transmitted X-ray intensity, I_0 is the initial X-ray intensity, and L is the

length of the X-ray path through the material. A reference material was used for quality control (QC) and comprised three layers: air, water, and aluminum consisting of a telescope-shaped cylinder with six steps (1–6 cm in diameter). The QC material was scanned after air calibration to check that the CT numbers were within QC ranges of $-1008 <$ CT number < -1002 for the air layer, $-2 <$ CT number < 7 for the water layer, and $2416 <$ CT number < 2499 for the aluminum layer. The LAC is a function of the chemical composition and density of the target material (Godel, 2013), meaning that XCT imaging provides information not only about density but also about chemical compositions (i.e., constituent elements) of the cores. For example, onboard lithological observations have suggested that the matrix of listvenite is composed of magnesite (density = 3037 kg/m^3: Yao et al. (2018) and quartz (density = 2650 kg/m^3: Mavko et al. (2020), whereas veins are inferred to be composed mainly of dolomite (density = 2880 kg/m^3: Mavko et al. (2020). However, CT numbers of the matrix in core section BT1B 49Z-1 (~3000) are lower than those of veins (~3400), which reflects the presence of calcium in dolomite, which has a higher atomic number and thus higher attenuation coefficient than those of other elements in magnesite and quartz (i.e., Mg, Si, C, and O).

Figure 3 shows histograms of CT numbers for slices taken at intervals of 100 mm along the Z-axis for the 100–600 mm core section of BT1B 49Z-1 and corresponding to the slices shown in Figure 2c–h. For quantitative evaluation of the mineral assemblage of the listvenite core, we used histograms for data taken from the center of the core cropped

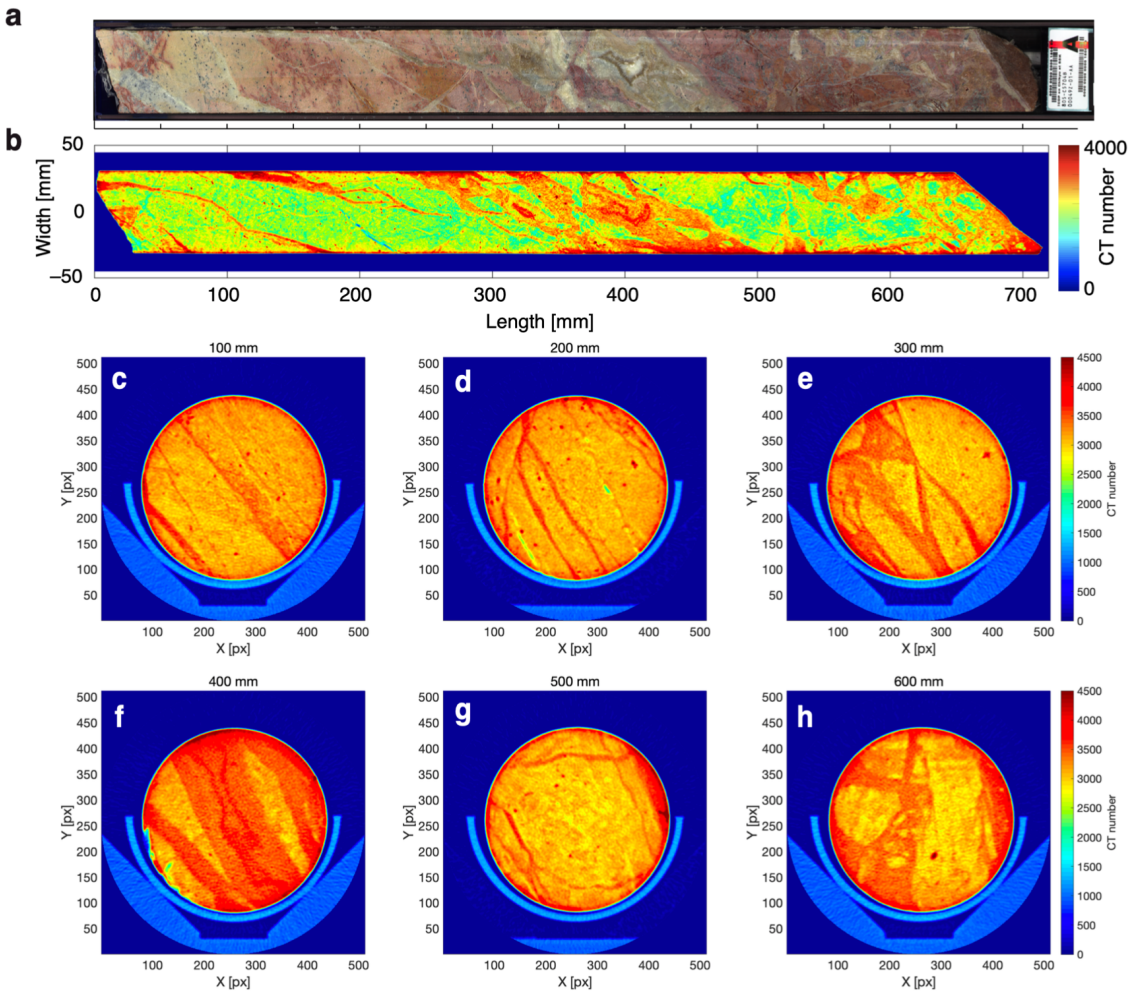

Figure 2. (a) MSCL-I image along the X–Z plane and (b) X-ray CT images along (b) the X–Z plane and (c–h) X–Y planes for intervals between 100 and 600 mm along the Z-axis of core section 49Z-1 from Hole BT1B.

in a circle with a radius of 100 pixels (i.e., 17.6 mm in radius). This data screening process removed the CT numbers of air and core tubes (CT number peaks of ~1000 and ~1300) and the regions affected by the X-ray hardening effect, which cover mostly the boundary between core sample and air. In Figure 3b, there are at least two peaks in each histogram, and the position and the height of these peaks change with position on the Z-axis of the core sample.

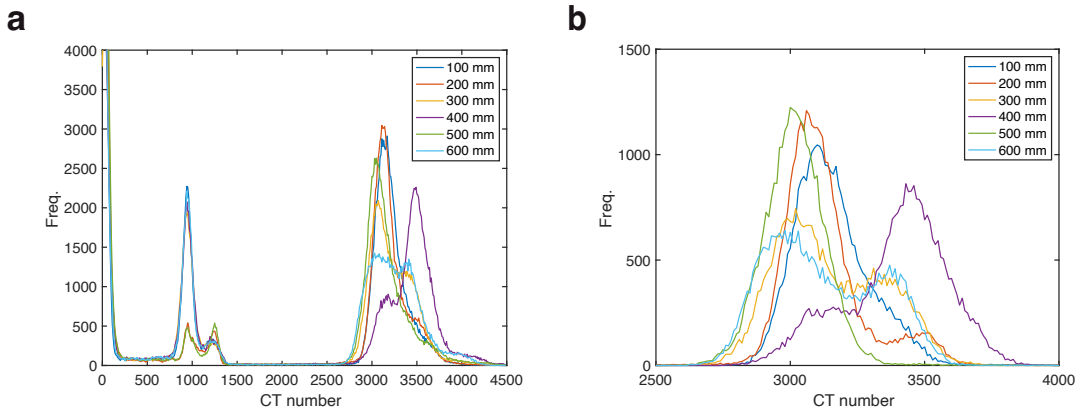

Figure 3. Histograms of CT number from images from Figure 2c–h for core section 49Z-1 from Hole BT1B. (a) Histograms of CT number for entire images for each X–Y slice along the Z-axis (i.e., depth). (b) Histograms of CT numbers for images cropped in a circle with a radius of 100 pixels for each X–Y slice along the Z-axis.

2.3. XRF mapping of the working half core surface using an XRF core scanner

To establish the relationship between XCT number and mineral species, we directly compared CT number with the element abundance measured by an XRF core scanner for the same locations. Twenty intervals of listvenite core were selected for non-destructive X-ray chemical analysis of the flat surface of the archive half core using the mapping mode of the XRF core scanner (Table S1). Detailed measurement conditions have been described in the initial report on the ICDP Oman Drilling Project (Kelemen et al., 2020). The operating conditions were a voltage of 30 kV, a beam current of 0.04 mA, a counting time of 60 s, a spot size 7 mm, and a spacing between spots of 5 mm.

Figure 4 shows examples of an MSCL-I image (a), an XCT image (b), and XRF-scanner element maps for SiO_2 (c), MgO (d), CaO (e), and Fe^*O (f) of the archive half core split surface at an interval of 200–550 mm along core section BT1B 49Z-1. Similar XCT and XRF maps from all other intervals of listvenite cores from Hole BT1B (Table S1) used in this study are presented in the Supplementary Information (Figures S2–S19).

These maps are useful for distinguishing relative element abundances and were used to identify mineralogical and lithological variability and compositional transitions. Data correction was performed to improve the raw output from the XRF scanner as described in Kelemen et al. (2020b). Data correction was conducted to allow comparison of the shore-based analysis at Southampton University, shipboard XRF analyses of BT1B core samples, and previous work (Falk & Kelemen, 2015). We considered only the weight fractions of SiO_2, MgO, CaO, and Fe^*O, and assumed that the sum of these four oxides should be 100%. Details of the data correction procedure are described in the method section in the initial report on the ICDP Oman Drilling Project (Kelemen et al., 2020a).

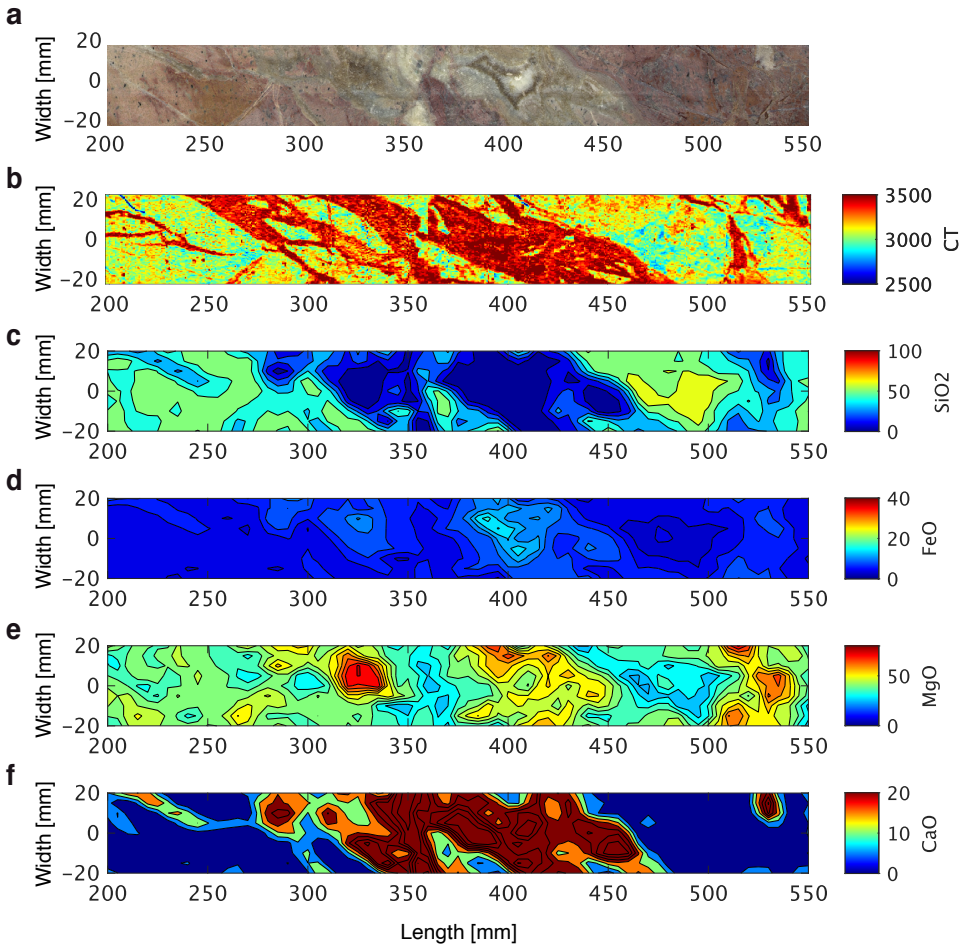

Figure 4. Comparison of (a) the MSCL-I image, (b) the XCT image, and (c) SiO_2, (d) FeO, (e) MgO, and (f) CaO chemical mapping from the XRF scanner for core section BT1B 49Z-1.

2.4. Comparison between CT number and XRF element composition

To determine the ideal CT numbers for quartz, magnesite, and dolomite with respect to the dimensions of drill cores and settings for the XCT scanner, composition maps (SiO_2, MgO, and CaO) from the XRF core scanner were compared with the CT number of the pseudo-archive half section (X–Z plane) image generated from the XCT image. To remove the CT hardening effect, which is an effect in which the CT number appears artificially high at the boundary between two material with extremely different CT numbers such as the boundary between air and minerals, we used those XCT and XRF data from the center of the core cropped in a circle with a radius of 100 pixels (35.2 mm in diameter) for comparison. A total of 865,415 data points for each element are plotted in Figure 5. Using these data, we determined the relationship of CT number with abundances of SiO_2, MgO, and CaO using multiple linear regression (MLR) analysis, which yielded the equation:

$$CT\ number = -5.16 \pm 0.10 \times SiO_2\ [wt.\%] - 3.83 \pm 0.10 \times MgO\ [wt.\%] + 1.26 \pm 0.10 \times CaO\ [wt.\%] + 3489.64 \pm 8.80 \quad (3).$$

These parameters obtained from MLR (Table S2) gave ideal CT numbers for quartz (SiO_2), magnesite ($MgCO_3$), and dolomite ($CaMg(CO_3)_2$) from the core of Hole BT1B of 2974.1 ± 18.9, 3106.4 ± 19.2, and 3415.5 ± 19.8, respectively (Table 1). These numbers are consistent with the CT numbers of rock samples of quartz, magnesite, and dolomite measured onboard D/V *Chikyu* (Kelemen et al., 2020b), but we were able to determine the positions of the peaks more strictly by additionally considering the confidence interval for the position of each peak.

It should be noted that we did not consider Fe and its related minerals in this study, because Fe can exist as Fe^{2+} and Fe^{3+} and thus in many mineral phases in listvenite (e.g., magnetite, hematite, Cr-spinel, and even siderite as an end-member of the magnesite–calcite–siderite solid solution).

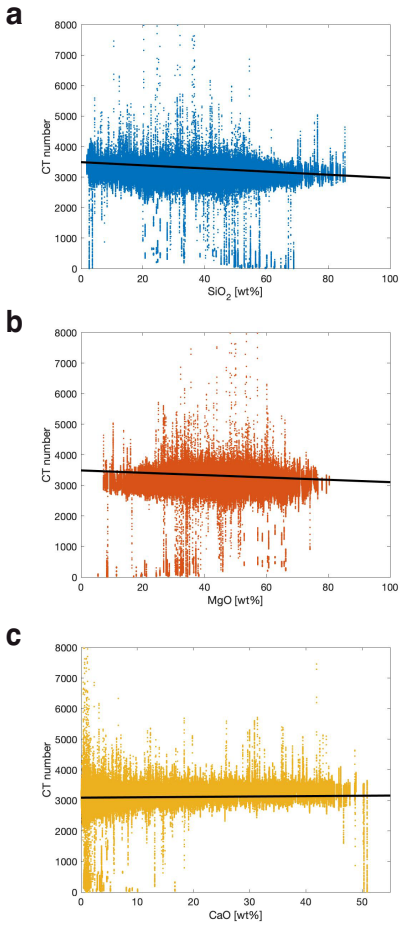

Figure 5. Comparisons of CT number with XRF chemical data for listvenite core samples from Hole BT1B. (a) CT number versus SiO_2, (b) CT number versus MgO, and (c) CT number versus CaO. Black lines in figures depict the linear relationship between XCT number and element fractions, whereas actual parameters of the relationship among XCT number and element fractions used for the downhole calculation are obtained using multiple linear regression (see section 2.4).

Table 1. Parameters used for the calculation for the downhole mineral fraction and physical properties.

Mineral	Chemical formula	CT number*	Density [kg/m3]	Bulk modulus (GPa)	Shear modulus (GPa)	V_P [km/s]**	V_S [km/s]**	λ [W/m/K]***
Quartz	SiO_2	2974.1 ± 18.9	2650	36.6	45.0	6.04	4.12	7.69
Magnesite	$MgCO_3$	3106.4 ± 19.2	3037	117.5	69.1	8.31	4.77	5.84
Dolomite	$CaMg(CO_3)_2$	3415.5 ± 19.8	2880	69.4	51.6	6.93	4.23	5.51

*CT number for dolomite is calculated from the CT number of 60.7% CaO + 39.3% MgO
**Reference for velocities: Quartz; Mavko et al., (2020), Magnesite; Yao et al., (2018), Dolomite; Mavko et al., (2020).
***Thermal conductivities from Clauser and Huenges (1995)

2.5. Fitting of peaks of each XCT slice image

Using the ideal CT numbers for quartz, magnesite, and dolomite (Table 1), we conducted peak fitting for all X–Y plane XCT images of the 200-m-long core BT1B,

249 which number more than 250,000 for the listvenite sections. An important assumption
250 used for calculating the mineral fractions of listvenite is that the CT number of a pixel
251 reflects the sum of the product of the volume fractions and the CT number of the different
252 minerals (and possibly the volume fraction of air) in the pixel. Therefore, a histogram of
253 the distribution of CT number in a CT image shows the volume fractions of minerals in
254 the core. For calculation of XCT data, we used MATLAB and its Image Processing
255 Toolbox and Curve Fitting Toolbox. The procedure for image analysis involved eight
256 steps, as follows:
257 1. X–Y plane 2D XCT data were saved as raw DICOM files and merged into a single X–
258 Y–Z 3D XCT dataset for each core section. 3D XCT data of each core section were
259 saved in a folder in MATLAB standard format (.mat).
260 2. A histogram of CT number for each X–Y plane image was calculated using the data
261 from the center of the core cropped in a circle with a radius of 100 pixels (e.g., Figure
262 3b).
263 3. Each histogram was fitted with three peaks (i.e., quartz, magnesite, and dolomite peaks),
264 assuming that the shape of the peaks follows a Gaussian distribution:
265
266 $$y = \sum_{i=1}^{3} a_i \exp\left[-\left(\frac{x-b_i}{c_i}\right)^2\right] \quad (4)$$
267
268 where a_i, b_i, and c_i are constants for quartz (i = 1), magnesite (i = 2), and dolomite (i =
269 3) peaks, respectively; and x is the XCT number. The position of each peak (e.g., b_i)
270 was fitted using the ideal CT numbers for quartz, magnesite, and dolomite as described
271 above in section 2.4. and considering the respective confidence intervals. The height
272 and width (i.e., a_i and c_i) of each peak were assumed to range from 0 to infinity for the

fitting process.

4. Fitting results [(values of a_i, b_i, and c_i and the coefficient of determination (R^2)] were saved in the workspace.

5. Volume fractions of quartz (n_1), magnesite (n_2), and dolomite (n_3) from the fitting parameters of the histogram were also calculated as follows:

$$n_i = a_i c_i / \sum_{i=1}^{3} a_i c_i \quad (5).$$

The volume fraction of each mineral was also saved in the workspace.

6. The pixels for which the CT number is lower than that of the lower side of the 99% confidence interval (2.5σ) of the quartz peak were considered for calculating porosity. Similarly, the pixels for which the CT number is higher than that of the higher side of the 99% confidence interval of the dolomite peak were considered for calculating the volume fraction of heavy minerals. A more detailed description of this procedure is given below in section 4.3.

7. Histogram peak fitting was continued for all X–Y CT images of a core section. Once the calculation for a section was finished, data were saved as a .mat file in a folder.

8. X–Y–Z CT data for a section and saved calculation results were deleted from the workspace, then new X–Y–Z CT data of another section were opened, with the process continuing through steps 2 to 7 until calculations for all core sections had been completed.

3. Results

3.1. Peak fitting results and downhole volumetric mineral fractions of listvenite from core BT1B

Figure 6 presents an example of the results of peak fitting from core section BT1B 49Z-1. Mineral fractions as a function of distance along the Z-axis (i.e., depth) inferred from XCT images indicate that matrix-rich parts are composed mainly of a quartz–magnesite mixture, whereas vein-rich parts are composed predominantly of dolomite (Figure 6b). This result is consistent with elemental mapping obtained from the XRF core scanner (Figure 4).

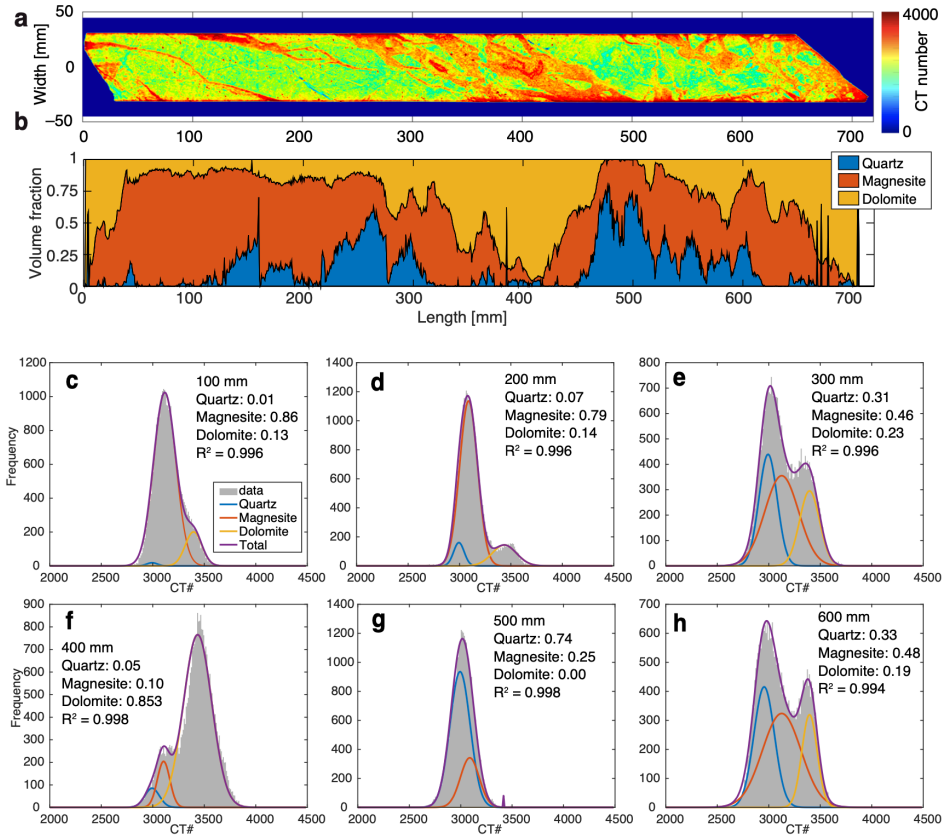

Figure 6. (a) XCT image and (b) calculated mineral fractions from XCT images of core section BT1B 49Z-1. (c–h) Examples of peak fitting results of XCT histograms at depths (core section Z-axis) of 100–600 mm.

Figure 7 shows the lithology of core BT1B, the downhole volume fractions of minerals, and the mole fraction of SiO_2, MgO, CaO, and CO_2 calculated from XCT data. Analytical results for which the R^2 value of fitting is $\geq$0.99 were used to calculate the mean mineral fractions for each core section for Figure 7b as well as the mean mole

fractions for each core section for Figure 7c. Results show that the mineral fractions are successfully solved from the XCT images in most core sections and that most of the listvenite section is composed of quartz and magnesite, except for the depth range of ~200–170 m, that is, within ~30 m above the basal thrust. In this deeper part of the core, dolomite is the dominant mineral phase, and the presence of minor quartz is detected from the XCT data. The downhole mean volume fractions of quartz, magnesite, and dolomite are 0.38, 0.49, and 0.13, respectively. These values correspond to downhole mean weight fractions for SiO_2, MgO, and CaO of 0.52, 0.42, and 0.06, respectively.

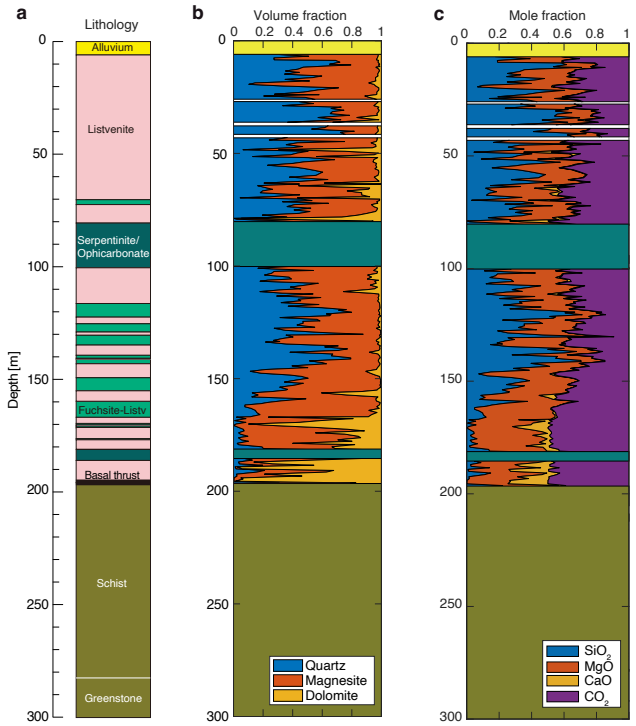

Figure 7. Downhole (a) lithology, (b) mineral volume fraction, and (c) element molar fractions (SiO_2, MgO, CaO, and CO_2) of listvenite for Hole BT1B.

3.2. Data refinement using R^2 values to calculate downhole mineral fractions

The quality of fit of the obtained XCT data depends on the condition of core samples (e.g., the number of open fractures because fracturing increases the air-mineral contact area resulting CT hardening effects), which in turn influences the calculated downhole mineral fractions. Figure 8 shows the degree to which the peak fitting results capture the

characteristics of the histograms of the XCT images. A fitting result with $R^2 = 0.90$ fails to adequately describe the histograms of the XCT images (Figure 8a). Figure 9a shows how the calculated total volume fraction of each mineral in Hole BT1B changes with respect to the adopted threshold R^2 value. Fitting results for $R^2 < 0.925$ tend to show a higher abundance of dolomite (Figure 9a) than those for $R^2 > 0.99$. The total quartz

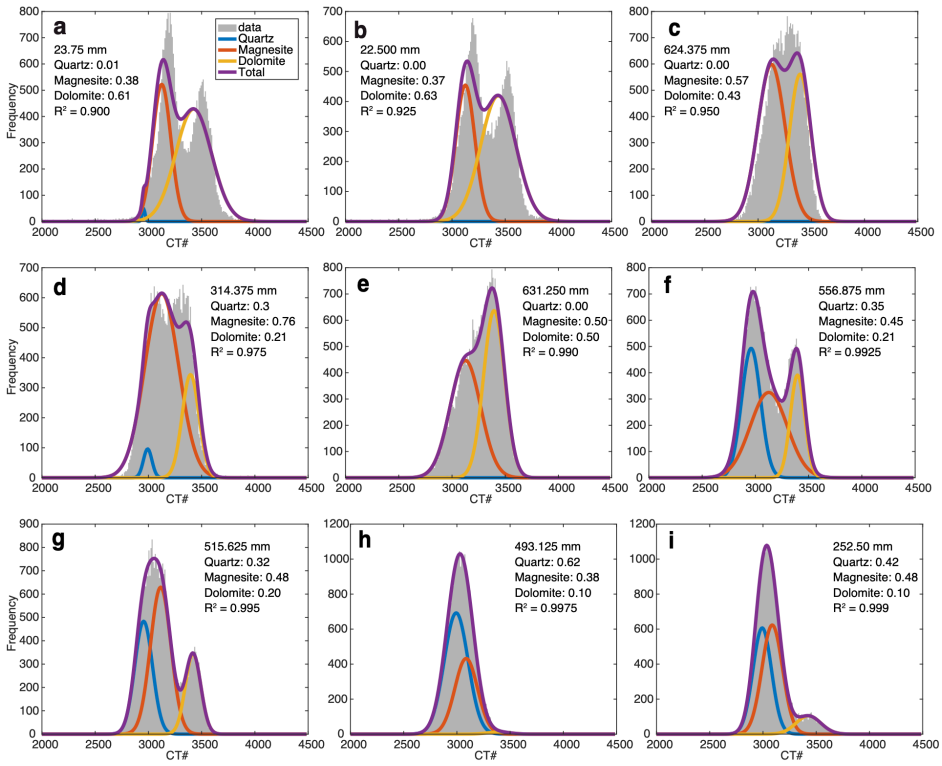

Figure 8. Examples of the changing appearance of histogram peak fitting results with different R^2 values. All histograms are for core section 49Z-1 of Hole BT1B.

fraction is nominally constant regardless of the threshold R^2 value, whereas the magnesite fraction increases and dolomite fraction decreases with increasing threshold R^2 value. This might reflect the fact that dolomite occurs mostly heterogeneously as veins, which tend to be located close to fractures, resulting in CT hardening. The presence of fractures or void spaces filled by air in the core sample also decreases the quality of the fitting. Alternatively, some calcite-rich veins might be present in the cores, which show higher

CT numbers than that of dolomite (CT number = ~4000; Kelemen et al., 2020b), whereas onboard microstructural and geochemical observations reveal that calcite or calcite-rich carbonate vein is minor (Kelemen et al., 2020b). Even if we applied such a tight threshold (R^2 ≥0.99), more than 50% of data (>125,000 XCT images) remain available for analysis (Figure 9b). Therefore, we use only the fitting results for R^2 values of ≥0.99 as a basis for discussion in Section 4.

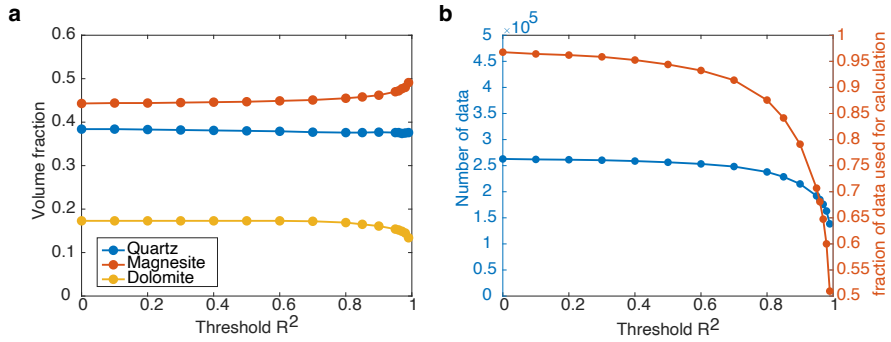

Figure 9. Data selection using threshold R^2 values of the histogram peak fitting results with respect to downhole mineral fractions evaluated from XCT images of entire listvenite sections from Hole BT1B. (a) Calculated volume mineral fractions as a function of threshold R^2 value. (b) Number and fraction of data used for calculating downhole mineral fractions as a function of threshold R^2 value.

4. Discussion

4.1. SiO_2–MgO–CaO fractions in listvenite from BT1B

Figure 7c presents the downhole mole fractions of SiO_2, MgO, CaO, and CO_2 from the mineral fractions estimated from XCT data for Hole BT1B. The downhole mean mole fractions of SiO_2, MgO, CaO, and CO_2 are 0.28, 0.33, 0.03, and 0.36, respectively. The abundance of MgO ranges from 0.2 to 0.5, and that of CO_2 increases slightly with increasing depth. The abundances of SiO_2 and CaO vary with depth more than that of MgO, and the variation in SiO_2 is larger than that in MgO, ranging between 0.1 and 0.8. The abundance of dolomite (i.e., CaO, as only one Ca-bearing mineral was considered in this study) shows a spiked distribution with depth, and its abundance increases downward

352 from ~40 m above the basal thrust (~160 m depth). In contrast, the abundance of quartz
353 decreases markedly downward from a depth of ~140 m, and dolomite becomes the most
354 abundant mineral downward from a depth of 170 m. These patterns could indicate that
355 the relative abundance of Si decreases owing to enrichment of Ca and CO_2 and/or loss of
356 Si by dissolution into fluid near the basal thrust. In fact, high fracture and vein densities
357 have been observed close to the basal thrust (Kelemen et al., 2020c). Therefore, the
358 heterogenous distributions of Si and Ca could indicate that the basal thrust acted as a
359 pathway for Ca- and CO_2-rich fluids.
360
361 **4.2. Comparison of CT data with geochemistry data from core samples**
362 Figure 10a–d shows a comparison between SiO_2, MgO, CaO, and CO_2 abundances
363 estimated from the XCT images and geochemical measurements on individual quarter-
364 core samples conducted onboard D/V *Chikyu* (Kelemen et al., 2020a; Kelemen et al.,
365 2020c). Geochemical data were calculated from the weight fractions of SiO_2, MgO, and
366 CaO estimated from XRF measurements using bead samples and the CO_2 weight fraction
367 from loss of ignition (LOI) measurements. The weight fraction of MgO from XCT is in
368 good agreement with that from geochemical measurements. The XRF data for SiO_2 and
369 CaO are less variable than the corresponding XCT data, especially for depths below 160
370 m. This could represent the effect of sample bias for the geochemical measurements,
371 given that analysis locations that were relatively intact and uniform could have been
372 chosen for XRF measurements, or a shift of CT numbers for the cores slightly toward
373 higher values because of the CT hardening effect between the quartz/magnesite matrix
374 and dolomite veins. Interestingly, mineral volume fractions from XCT data show good
375 agreement with those obtained from thin-section observations (Figure 10f and g).

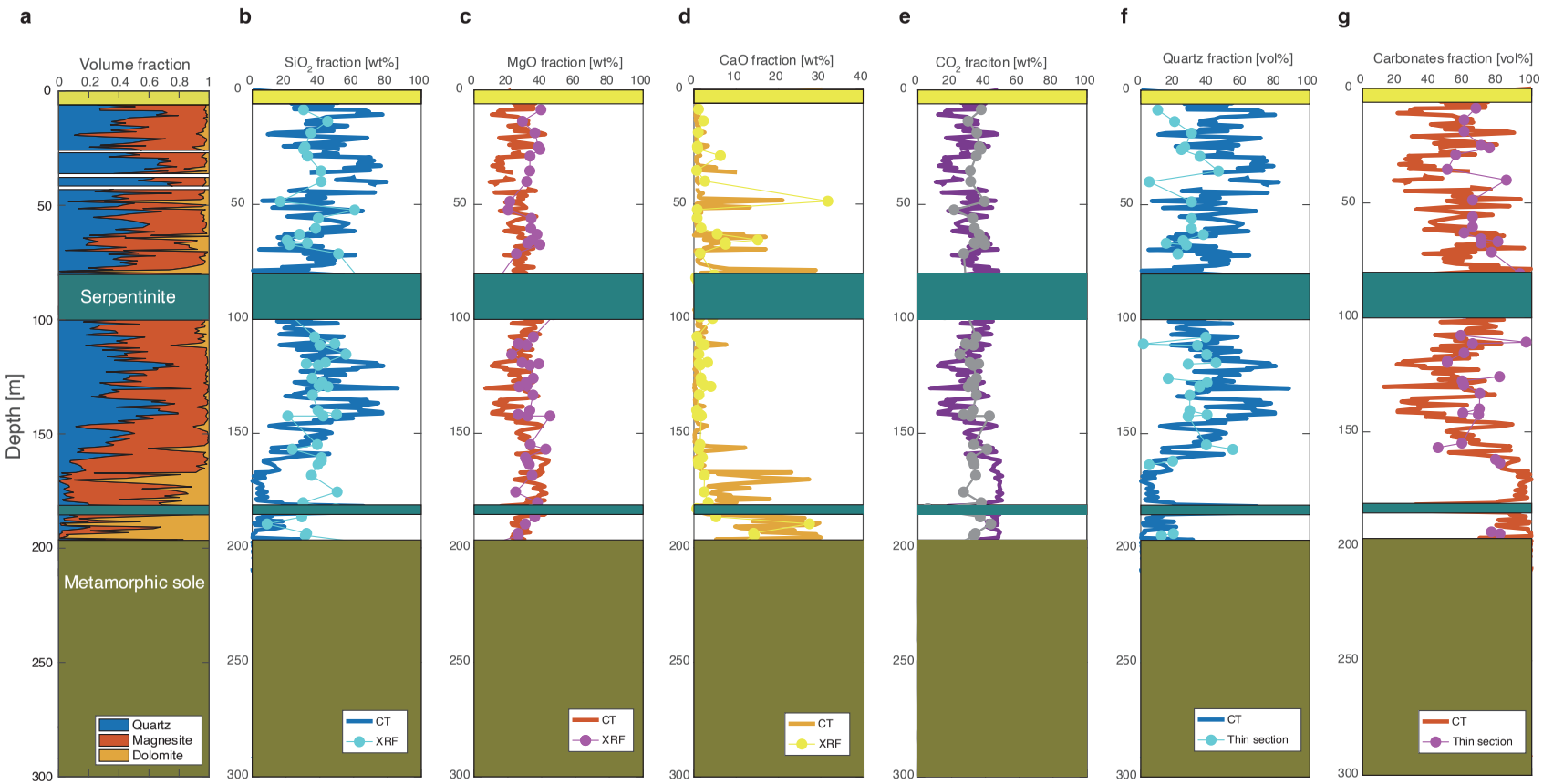

Figure 10. Downhole element and mineral fractions estimated from XCT images and from geochemical measurements of individual samples for Hole BT1B. (a) Downhole volume fractions of quartz, magnesite, and dolomite. (b–e) Element fractions of SiO_2, MgO, CaO, and CO_2, showing a comparison between data from XCT images and from XRF and LOI measurements. (f and g) Comparison of mineral fractions estimated from XCT images and from thin section observations under an optical microscope.

4.3. Comparison of CT data with physical property data core samples

Physical properties of the listvenite core sections from Hole BT1B can also be calculated from mineral fractions estimated from XCT images. We estimated porosity and the volume fraction of high-density (heavy) minerals from XCT images (Figure 11b and c). Porosity and the heavy mineral (HM) fraction were calculated from the fitting of XCT images (see also section 2.5. above). Porosity was determined from the residual of the XCT histogram after fitting the histogram with the three peaks for quartz, magnesite, and dolomite considering the pixels for which CT number was lower than that of the lower part of the 99% confidence interval (2.5σ) of the quartz peak. Similarly, the HM fraction was also determined from the residual of the XCT histogram after fitting, considering the pixels for which CT number was higher than that of the higher part of the 99% confidence interval of the dolomite peak. In addition to porosity, the density, thermal conductivity, and seismic velocity were calculated from the XCT mineral fractions. For calculations, we adopted standard values for the physical properties (density, elastic constants, and thermal conductivity) of quartz, magnesite, and dolomite, as summarized in Table 1.

The bulk density of listvenite was determined from the density of each mineral and the density of water multiplied by volume fractions, similar to the measurements for bulk density made onboard D/V *Chikyu* using individual water-saturated samples (Kelemen et al., 2020a). Seismic velocities and thermal conductivities were calculated on the basis of the Voigt–Reuss–Hill averages and series-parallel models of each mineral, respectively. The effects of pore spaces on seismic velocity and thermal conductivity depend not only on the porosity value but also on pore geometry (Brantut & David, 2018; Clauser & Huenges, 1995; O'Connell & Budiansky, 1974), and thus the relationships among these properties are complex. Therefore, we plotted downhole seismic velocity

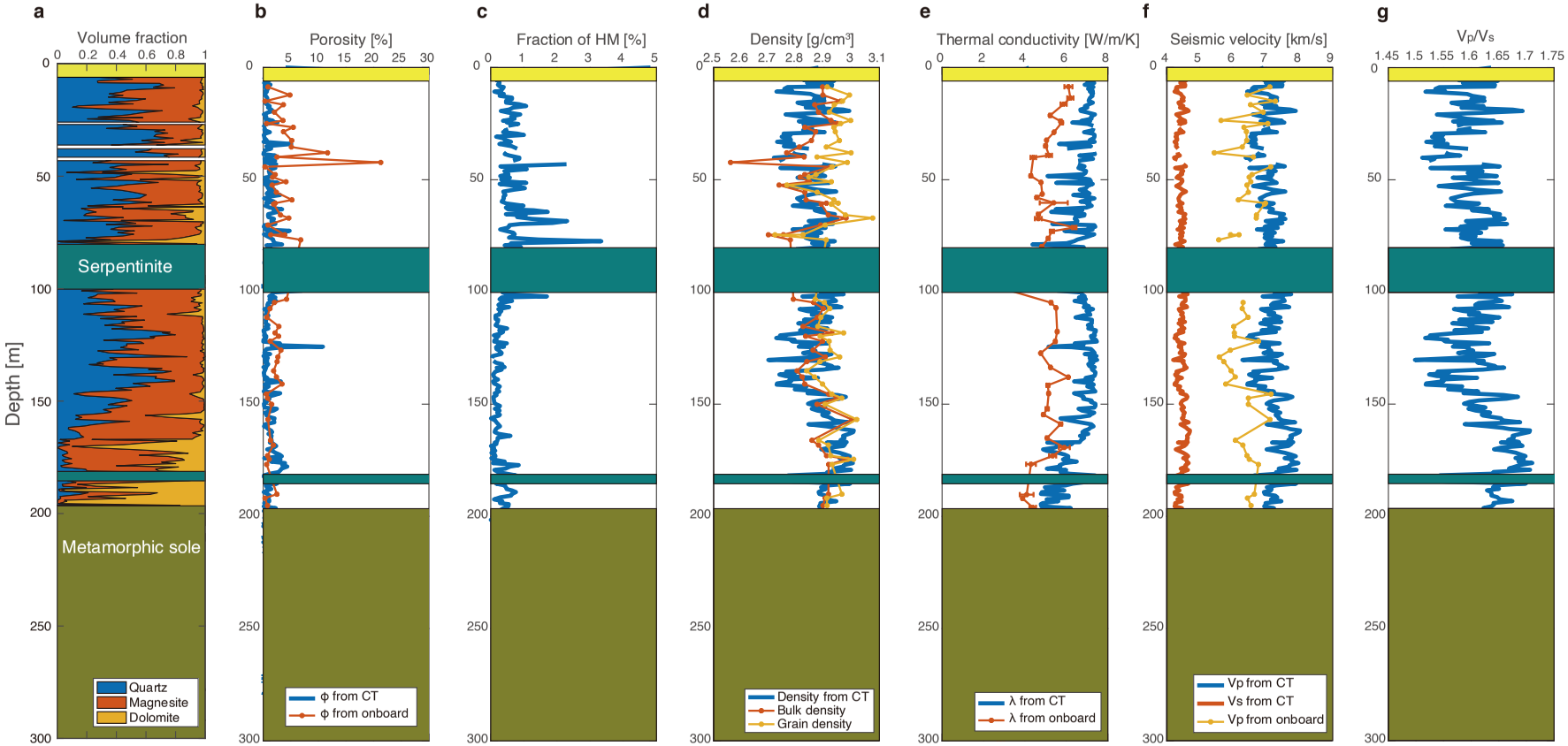

Figure 11. Downhole variation in physical property data from XCT images and from physical property measurements of individual samples for Hole BT1B. (a) Downhole volume fractions of quartz, magnesite, and dolomite. (b) Comparison of downhole porosity estimated from XCT images and from analysis of individual samples. (c) Volume fraction of heavy minerals (HM). (d–f) Comparisons of downhole (d) density, (e) thermal conductivity (λ), and (f) seismic velocity (p-wave velocity: Vp and s-wave velocity: Vs) estimated from XCT images and from analysis of individual samples.

and thermal conductivity calculated from XCT images and assuming no effect of porosity on these properties (Figure 11e and f).

Downhole porosity estimated from the CT images is slightly lower than that measured using individual samples (Figure 13b). This might be due to not considering pore space in this study, as we used results for fitting with $R^2 > 0.99$, and thus the high porosity region might have been removed by this procedure owing to the low CT number of air (−1000). For most of the listvenite section, porosity is less than 3%. The upper listvenite and the lowermost listvenite subsections show slightly higher porosity values. This may be explained by the density of cataclasite measured during the core description on board D/V *Chikyu* (Kelemen et al., 2020c). The HM fraction is ~2 vol.% in the upper listvenite subsection and <1 vol.% in the lower listvenite subsection. In the archive core half section, surfaces show that the color of the upper listvenite subsection is more reddish (a high R value in RGB (red-green-blue color scale) and high a* in the La*b* color scale; Kelemen et al., 2020c) than the lowermost listvenite subsection. The relatively high HM fraction in the upper listvenite subsection might be due to a high hematite (Fe_2O_3) fraction in the listvenite matrix, as hematite typically shows a rusty red color. Some peaks of the high HM fraction correspond to enrichment of Cr-spinel (e.g., core section 45Z-3 at100 m depth; see VCD of Hole BT1B; Kelemen et al. (2020c).

Figure 11d shows a downhole comparison of density estimated from XCT images and physical property measurements conducted onboard D/V *Chikyu*. Values of density calculated from XCT images are reasonably consistent with the sample density measurements. The mean density is ~2850 kg/m^3 through the depth range of 10–140 m and increases slightly to ~2950 kg/m^3 below a depth of 140 m. This slight increase in density can be explained by the decrease in the fraction of quartz and the corresponding

increase in the fraction of dolomite.

Figure 11e shows a downhole comparison of thermal conductivity estimated from XCT images and physical property measurements conducted onboard D/V *Chikyu*. The overall pattern of the thermal conductivity profile calculated from XCT images is similar to that given by the sample measurements, although the values are shifted lower by ~2 W/m/K compared with the sample measurements. This difference can be explained by the effects of porosity and pore geometry (e.g., the aspect ratio of cracks), given that the thermal conductivity of water is about an order of magnitude lower than those of minerals constituting the listvenite, and pore connectivity has a significant effect on bulk thermal conductivity. Alternatively, the thermal conductivity values of each mineral in listvenite in Hole BT1B might differ slightly from reference values reported in the literature (Diment and Pratt (1988); Horai (1971); Newnham (2005) summarized in Clauser and Huenges (1995)). Nevertheless, regardless of any of the above effects, the thermal conductivity of listvenite (~6 W/m/K) is clearly higher than those of dry peridotite (~5 W/m/K) and serpentinite (~3 W/m/K). The downhole thermal conductivity of listvenite decreases below a depth of ~150 m on account of the decrease in the quartz fraction, as quartz has the highest thermal conductivity (~8 W/m/K) of the various minerals in listvenite.

Figure 11f presents a comparison of seismic velocity estimated from XCT images and physical property measurements conducted onboard D/V Chikyu. The downhole average physical properties of listvenite from Hole BT1B is summarized in Table 2. The P-wave velocity of listvenite from XCT images is about 7 km/s and increases slightly to ~7.6 km/s below a depth of ~150 m, probably due to the decrease in the fraction of quartz (6.04 km/s; Mavko et al. (2020) and the corresponding increase in the fraction of dolomite

(6.93 km/s; Mavko et al. (2020). The P-wave velocity estimated from XCT images, a procedure that assumes 0% porosity, is systematically higher than that determined from onboard sample measurements. Since seismic velocity is highly sensitive to thin cracks (e.g., O'Connell & Budiansky, 1974; Kuster & Toksöz, 1974), this difference can be explained by a few percent of porosity in the listvenite cores as calculated from the XCT images (Figure 11b). In comparison with the seismic velocities of peridotite (Vp = ~8.0 km/s, Vs = ~4.5 km/s), lizardite (Vp = ~4.8 km/s, Vs = ~2.3 km/s), and antigorite serpentinite (Vp = ~6.5 km/s, Vs = ~3.6 km/s; Christensen, 2004), the values of Vp and Vs of listvenite lie between those of peridotite and antigorite serpentinite. In addition, the seismic velocity of listvenite is close to that of 10%–30% serpentinized (lizardite–chrysotile) peridotite. The average Vp/Vs ratio of listvenite is ~1.6. This value is slightly smaller than that of peridotite and antigorite serpentinite (~1.8) while significantly smaller than that of lizardite-chrisotile serpentinite (Christensen, 2004). These results indicate that listvenite could be hard to identify using seismic observations, even if mantle carbonation (i.e., listvenitization) occurs widely beneath the sea floor and subduction zones.

Table 2. Average mineral fraction and physical properties of listvenite from Hole BT1B calculated from XCT data and from onboard measurements

	Quartz [vol%]	Magnesite [vol%]	Dolomite [vol%]	Porosity [vol%]	Heavy minerals [vol%]	Density [kg/m^3]	λ [W/m/K]*	V_P [km/s]	V_S [km/s]	V_P/V_S
CT data	37.6	49.1	13.4	1.15	0.44	2871	6.14	7.15	4.44	1.61
Onborad measurements	35.5#	54.5#	10.1#	2.9	0.53#	2860/2920$	5.16	6.41	–	–

*Thermal conductivity
data from onboard XRD measurements
$ Bulk density and grain density

4.4. Implications for fluid flow of CO_2-rich fluid and material transfer at the subduction zone

Figure 12a shows the mole fraction of MgO as a function of mole fraction of SiO_2 (mean values of each core section in Hole BT1B). Data for $SiO_2 < 0.4$ show scatter away from predicted trends, reflecting Mg addition/loss and/or Si addition/loss (Falk &

Kelemen, 2015). These data correspond to dolomite-rich sections and are thus located mostly near the basal thrust. Figure 12b shows a ternary plot of SiO_2–MgO–CaO mole fractions of listvenite from Hole BT1B. The SiO_2:MgO:CaO ratio is 43:51:5, and the Mg/Si ratio estimated from XCT images is 1.19. The SiO_2:MgO:CaO ratio and the Mg/Si ratio is nominally consistent with onboard geochemical data (SiO_2:MgO:CaO = 41:54:5, Mg/Si = ~1.31: values ignoring the other elements; Kelemen et al., 2020c), whereas the Mg/Si ratio of listvenite is lower than that of Oman harzburgite (SiO_2:MgO:CaO = 39:60:1, Mg/Si ~1.53: values ignoring the other elements; Godard et al., 2000). These difference of the SiO_2:MgO:CaO and the Mg/Si ratios between Oman listvenite and harzburgite suggest that Mg loss and/or Si addition, as well as Ca addition, occurred during carbonation (listvenitization) as suggested by Falk and Kelemen (2015).

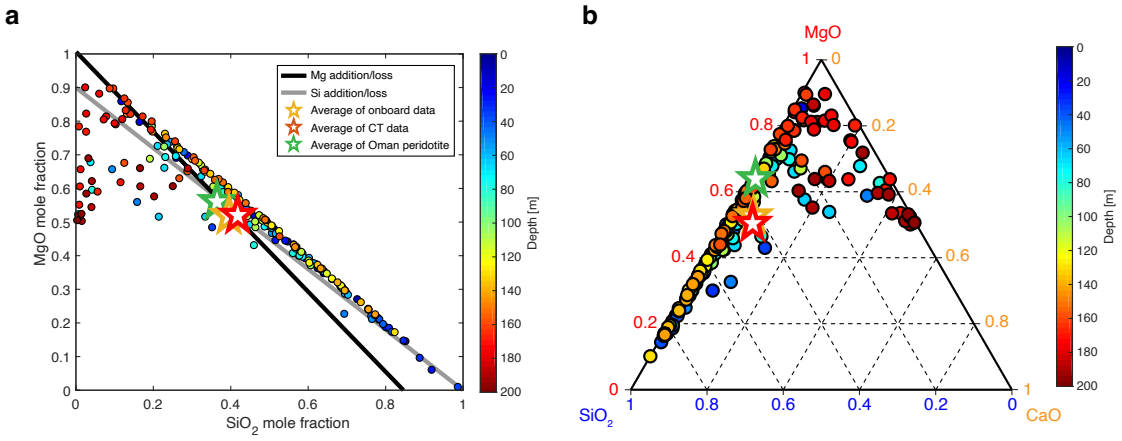

Figure 12. Element fractions for Hole BT1B. (a) Mole fraction of MgO as a function of mole fraction of SiO_2. Color of small circles indicates down-core depth. (b) Ternary plot of SiO_2–MgO–CaO fractions from XCT images. Color of small circles indicates down-core depth. Red, orange, and green stars indicate mean values of XCT data, onboard discrete XRF data, and results for Oman peridotite outcrops (Godard et al., 2000; Takazawa et al., 2003).

Downhole mineral fractions inferred from XCT images indicate that dolomite occurs in veins and is located mostly near the basal thrust. The abundance of Ca in Oman

peridotite is low (<1 wt.% for harzburgite, Godard et al., 2000; <3 wt.% for lherzolite, Takazawa et al., 2003); therefore, Ca might have been supplied from fluids flowing along the basal thrust. Ishikawa et al. (2005) reported that the metamorphic sole close to the basal thrust is enriched with fluid-mobile elements such as B, Rb, K, and Ba, and argued that these elements are traces of fluid flow along the plate boundary. Although the chemical composition of the fluid might have been different from them during the obduction, and the carbonation of the Oman peridotite occurred at a low temperature (<250 °C; Benlich et al., 2020), it is still possible that the basal thrust (i.e., the plate boundary thrust fault) acted as a pathway for Ca- and CO_2-rich fluids into the Oman peridotite during the entire stage of obduction of the ophiolite, and potentially even before the obduction.

Structural observations of listvenite cores from BT1B suggest that the carbonation (i.e., listvenitization) occurred after the hydration (i.e., serpentinization) of peridotite in Oman ophiolite (Kelemen et al., 2020b). This indicates that the physical property, especially seismic velocities, of altering/altered mantle evolves with a complex manner with different degrees of carbonation and hydration. For example, the carbonation of fresh mantle peridotite decreases the Vp/Vs ratio from 1.8 to 1.6, which is in the opposite sense of the change of the Vp/Vs ratio of mantle peridotite by “typical alteration” meaning hydration (Figure 13). This kind of change in seismic property is more pronounced in the case of the carbonation of lizardite serpentinite; the Vp/Vs ratio changes from 2.0 to 1.6 as observed in the Oman ophiolite in this study. This suggests that a significant volume of listvenite (i.e., CO_2), which can be overlooked by seismic observations alone, could be subducting from the subduction zones. We emphasize that magnesite is potentially stable even at the lower mantle (Biellmann et al., 1993), listvenite can be a major host for carbon

in the entire mantle.

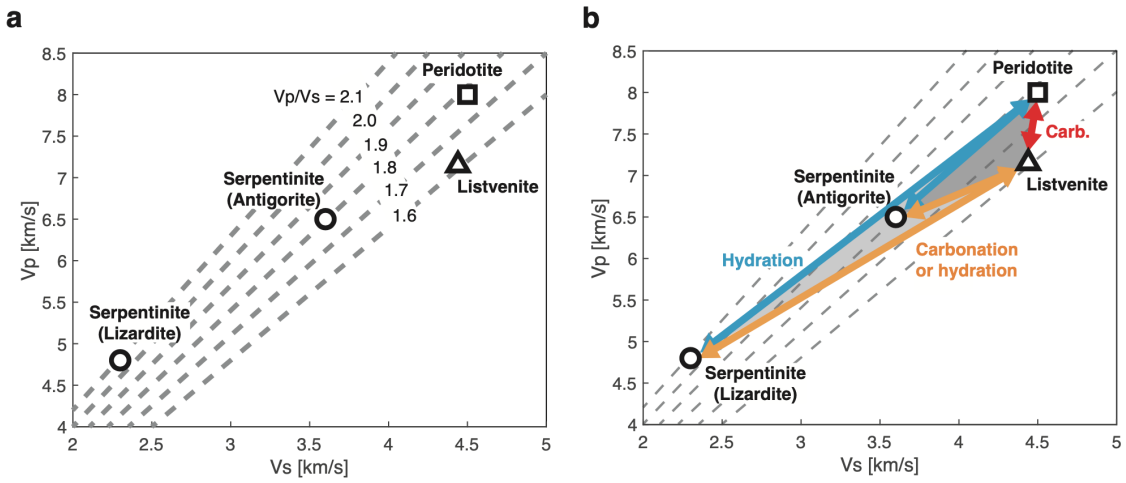

Figure 13. (a) P-wave velocity (Vp), S-wave velocity (Vs) and Vp/Vs ratio of listvenite (this study), peridotite, lizardite serpentinite and antigorite serpentinite (Christensen, 2004). Vertical and horizontal axes are Vp and Vs, respectively. Gray dashed lines indicate Vp/Vs ratio from 1.6 to 2.1. (b) Similar to Fig. 13a but with possible changes of seismic velocities by hydration and carbonation of listvenite, serpentinites and peridotite. Carb.: carbonation.

5. Conclusion

We evaluated the quartz–magnesite–dolomite fraction of listvenite drilled at Oman Drilling Project Hole BT1B from X-ray CT core images. For most core sections, XCT data indicate that the matrix of listvenite is composed of magnesite and quartz, consistent with discrete XRD and XRF data. Veins are composed mostly of dolomite. Downhole variation in the fraction of dolomite in Hole BT1B indicates that the basal thrust could have acted as a pathway for Ca-, Si-, and CO_2-rich fluids during carbonation. Vp, Vs and density of listvenite is relatively close to that of peridotite, but very different form serpentinite. A significant volume of listvenite (i.e., CO_2), which are being overlooked by seismic observations alone, could be subducting from the subduction zones to the deep of Earth's interior.

Acknowledgments

We thank laboratory technicians from Marine Works Japan Ltd. who measured X-ray CT images of core samples amounting to more than 2400 m in total during the project. We also thank Y. Kubo, T. Ishikawa, and I. Katayama for informative discussions. This research was supported by the Japan Society for the Promotion of Science (18H01318 to K. Okazaki and 18H01321 to N. Abe). This research used samples and/or data provided by the Oman Drilling Project. The Oman Drilling Project (OmanDP) was made possible by combined funds from the International Continental Scientific Drilling Project (ICDP; Kelemen, Matter, Teagle Lead PIs), the Sloan Foundation – Deep Carbon Observatory (Grant 2014-3-01, Kelemen PI), the National Science Foundation (NSF-EAR-1516300, Kelemen lead PI), NASA – Astrobiology Institute NNA15BB02A, Templeton PI), the German Research Foundation (DFG: KO 1723/21-1, Koepke PI), the Japanese Society for the Promotion of Science (JSPS KAKENHI: 16H06347, Michibayashi PI; and 16H02742, Takazawa PI), the European Research Council (Adv: no.669972; Jamveit PI), the Swiss National Science Foundation (SNF:20FI21_163073, Früh-Green PI), JAMSTEC, the TAMU-JR Science Operator, and contributions from the Sultanate of Oman Ministry of Regional Municipalities and Water Resources, the Oman Public Authority of Mining, Sultan Qaboos University, CRNS-Univ. Montpellier II, Columbia University of New York, and the University of Southampton.

Data availability

All raw XCT and XRF data used in this study are archived on the ICDP website (https://www.icdp-online.org/projects/world/asia/oman/details/) and have already been

549 published in the initial report on the ICDP Oman Drilling Project
550 (http://publications.iodp.org/other/Oman/OmanDP.html). MATLAB codes and analytical
551 results of this study are archived in ZENODO (doi: 10.5281/zenodo.4555143).
552
553 **Figure captions**
554
555 **Figure 1.** Principal lithologies of recovered core samples from Hole BT1B.
556
557 **Figure 2.** (a) MSCL-I image along the X–Z plane and (b) X-ray CT images along (b) the
558 X–Z plane and (c–h) X–Y planes for intervals between 100 and 600 mm along the Z-axis
559 of core section 49Z-1 from Hole BT1B.
560
561 **Figure 3.** Histograms of CT number from images from Figure 2c–h for core section 49Z-
562 1 from Hole BT1B. (a) Histograms of CT number for entire images for each X–Y slice
563 along the Z-axis (i.e., depth). (b) Histograms of CT numbers for images cropped in a
564 circle with a radius of 100 pixels for each X–Y slice along the Z-axis.
565
566 **Figure 4.** Comparison of (a) the MSCL-I image, (b) the XCT image, and (c) SiO_2, (d)
567 FeO, (e) MgO, and (f) CaO chemical mapping from the XRF scanner for core section
568 BT1B 49Z-1.
569
570 **Figure 5.** Comparisons of CT number with XRF chemical data for listvenite core samples
571 from Hole BT1B. (a) CT number versus SiO_2, (b) CT number versus MgO, and (c) CT
572 number versus CaO. Black lines in figures depict the linear relationship between XCT

573 number and element fractions, whereas actual parameters of the relationship among XCT
574 number and element fractions used for the downhole calculation are obtained using
575 multiple linear regression (see section 2.4).
576
577 **Figure 6.** (a) XCT image and (b) calculated mineral fractions from XCT images of core
578 section BT1B 49Z-1. (c–h) Examples of peak fitting results of XCT histograms at depths
579 (core section Z-axis) of 100–600 mm.
580
581 **Figure 7.** Downhole (a) lithology, (b) mineral volume fraction, and (c) element molar
582 fractions (SiO_2, MgO, CaO, and CO_2) of listvenite for Hole BT1B.
583
584 **Figure 8.** Examples of the changing appearance of histogram peak fitting results with
585 different R^2 values. All histograms are for core section 49Z-1 of Hole BT1B.
586
587 **Figure 9.** Data selection using threshold R^2 values of the histogram peak fitting results
588 with respect to downhole mineral fractions evaluated from XCT images of entire
589 listvenite sections from Hole BT1B. (a) Calculated volume mineral fractions as a function
590 of threshold R^2 value. (b) Number and fraction of data used for calculating downhole
591 mineral fractions as a function of threshold R^2 value.
592
593 **Figure 10.** Downhole element and mineral fractions estimated from XCT images and
594 from geochemical measurements of individual samples for Hole BT1B. (a) Downhole
595 volume fractions of quartz, magnesite, and dolomite. (b–e) Element fractions of SiO_2,
596 MgO, CaO, and CO_2, showing a comparison between data from XCT images and from

597 XRF and LOI measurements. (f and g) Comparison of mineral fractions estimated from
598 XCT images and from thin section observations under an optical microscope.
599
600 **Figure 11.** Downhole variation in physical property data from XCT images and from
601 physical property measurements of individual samples for Hole BT1B. (a) Downhole
602 volume fractions of quartz, magnesite, and dolomite. (b) Comparison of downhole
603 porosity estimated from XCT images and from analysis of individual samples. (c) Volume
604 fraction of heavy minerals (HM). (d–f) Comparisons of downhole (d) density, (e) thermal
605 conductivity (λ), and (f) seismic velocity (p-wave velocity: Vp and s-wave velocity: Vs)
606 estimated from XCT images and from analysis of individual samples.
607
608 **Figure 12.** Element fractions for Hole BT1B. (a) Mole fraction of MgO as a function of
609 mole fraction of SiO_2. Color of small circles indicates down-core depth. (b) Ternary plot
610 of SiO_2–MgO–CaO fractions from XCT images. Color of small circles indicates down-
611 core depth. Red, orange, and green stars indicate mean values of XCT data, onboard
612 discrete XRF data, and results for Oman peridotite outcrops (Godard et al., 2000;
613 Takazawa et al., 2003).
614
615 **Figure 13.** (a) P-wave velocity (Vp), S-wave velocity (Vs) and Vp/Vs ratio of listvenite
616 (this study), peridotite, lizardite serpentinite and antigorite serpentinite (Christensen,
617 2004). Vertical and horizontal axes are Vp and Vs, respectively. Gray dashed lines
618 indicate Vp/Vs ratio from 1.6 to 2.1. (b) Similar to Fig. 13a but with possible changes of
619 seismic velocities by hydration and carbonation of listvenite, serpentinites and peridotite.
620 Carb.: carbonation.

References

Abers, G. A., Nakajima, J., van Keken, P. E., Kita, S., & Hacker, B. R. (2013). Thermal–petrological controls on the location of earthquakes within subducting plates. *Earth and Planetary Science Letters, 369-370*, 178-187. https://doi.org/10.1016/j.epsl.2013.03.022

Audet, P., Bostock, M. G., Christensen, N. I., & Peacock, S. M. (2009, Jan 1). Seismic evidence for overpressured subducted oceanic crust and megathrust fault sealing. *Nature, 457*(7225), 76-78. https://doi.org/10.1038/nature07650

Baker, D. R., Mancini, L., Polacci, M., Higgins, M. D., Gualda, G., Hill, R., & Rivers, M. (2012). An introduction to the application of X-ray microtomography to the three-dimensional study of igneous rocks. *Lithos, 148*, 262-276.

Beinlich, A., Plümper, O., Boter, E., Müller, I., Kourim, F., Ziegler, M., Harigane, Y., Lafay, R., Kelemen, P., & Team, O. D. P. S. (2020). Ultramafic rock carbonation: Constraints from listvenite core BT1B, Oman Drilling Project. *Journal of Geophysical Research: Solid Earth, 125*(6), e2019JB019060.

Biellmann, C., Gillet, P., Peyronneau, J., & Reynard, B. (1993). Experimental evidence for carbonate stability in the Earth's lower mantle. *Earth and Planetary Science Letters, 118*(1-4), 31-41.

Brantut, N., & David, E. C. (2018). Influence of fluids on VP/VS ratio: increase or decrease? *Geophysical Journal International, 216*(3), 2037-2043.

Christensen, N. I. (2004). Serpentinites, peridotites, and seismology. *International Geology Review, 46*(9), 795-816.

Clauser, C., & Huenges, E. (1995). Thermal conductivity of rocks and minerals. *Rock physics & phase relations: a handbook of physical constants*, 105-126.

Dilek, Y., & Furnes, H. (2011). Ophiolite genesis and global tectonics: Geochemical and tectonic fingerprinting of ancient oceanic lithosphere. *Geological Society of America Bulletin, 123*(3-4), 387-411. https://doi.org/10.1130/B30446.1

656
657 Diment, W. H., & Pratt, H. R. (1988). *Thermal conductivity of some rock-forming minerals: A*
658 *tabulation*. US Geological Survey.
659
660 Expedition 343/343T Scientists. (2013). Expedition 343/343T summary. In Chester, F.M., Mori,
661 J., Eguchi, N., Toczko, S., and the Expedition 343/343T Scientists, Proc. IODP,
662 343/343T: Tokyo (Integrated Ocean Drilling Program Management International, Inc.).
663 *Proc. IODP, 343/343T*. https://doi.org/doi:10.2204/iodp.proc.343343T.101.2013
664
665 Falk, E. S., & Kelemen, P. B. (2015). Geochemistry and petrology of listvenite in the Samail
666 ophiolite, Sultanate of Oman: complete carbonation of peridotite during ophiolite
667 emplacement. *Geochimica et Cosmochimica Acta, 160*, 70-90.
668
669 GE healthcare. (2013). *Discovery CT750 User Manual*.
670
671 Godard, M., Jousselin, D., & Bodinier, J.-L. (2000). Relationships between geochemistry and
672 structure beneath a palaeo-spreading centre: a study of the mantle section in the Oman
673 ophiolite. *Earth and Planetary Science Letters, 180*(1-2), 133-148.
674
675 Godel, B. (2013). High-resolution X-ray computed tomography and its application to ore deposits:
676 From data acquisition to quantitative three-dimensional measurements with case studies
677 from Ni-Cu-PGE deposits. *Economic Geology, 108*(8), 2005-2019.
678
679 Hacker, B., & Mosenfelder, J. (1996). Metamorphism and deformation along the emplacement
680 thrust of the Samail ophiolite, Oman. *Earth and Planetary Science Letters, 144*(3-4), 435-
681 451.
682
683 Hansen, L. D., Dipple, G. M., Gordon, T. M., & Kellett, D. A. (2005). Carbonated serpentinite
684 (listwanite) at Atlin, British Columbia: A geological analogue to carbon dioxide
685 sequestration. *The Canadian Mineralogist, 43*(1), 225-239.
686
687 Horai, K. i. (1971). Thermal conductivity of rock - forming minerals. *Journal of Geophysical*
688 *Research, 76*(5), 1278-1308.
689
690 Ishikawa, T., Fujisawa, S., Nagaishi, K., & Masuda, T. (2005). Trace element characteristics of the
691 fluid liberated from amphibolite-facies slab: Inference from the metamorphic sole beneath

692 the Oman ophiolite and implication for boninite genesis. *Earth and Planetary Science*
693 *Letters, 240*(2), 355-377.
694
695 Kamiya, S. i., & Kobayashi, Y. (2000). Seismological evidence for the existence of serpentinized
696 wedge mantle. *Geophysical Research Letters, 27*(6), 819-822.
697
698 Kelemen, P. B., Matter, J., Streit, E. E., Rudge, J. F., Curry, W. B., & Blusztajn, J. (2011). Rates
699 and mechanisms of mineral carbonation in peridotite: natural processes and recipes for
700 enhanced, in situ CO2 capture and storage. *Annual Review of Earth and Planetary*
701 *Sciences, 39*, 545-576.
702
703 Kelemen, P. B., Matter, J. M., Teagle, D. A., Coggon, J. A., & Team, t. O. D. P. S. (2020a). Methods
704 and explanatory notes. In Kelemen, P.B., Matter, J.M., Teagle, D.A.H., Coggon, J.A., et
705 al., Proceedings of the Oman Drilling Project: College Station, TX (International Ocean
706 Discovery Program). https://doi.org/https://doi.org/10.14379/OmanDP.proc.2020
707
708 Kelemen, P. B., Matter, J. M., Teagle, D. A., Coggon, J. A., & Team, t. O. D. P. S. (2020b).
709 Proceedings of the Oman Drilling Project: College Station, TX (International Ocean
710 Discovery Program). https://doi.org/https://doi.org/10.14379/OmanDP.proc.2020
711
712 Kelemen, P. B., Matter, J. M., Teagle, D. A., Coggon, J. A., & Team, t. O. D. P. S. (2020c). Site
713 BT1: fluid and mass exchange on a subduction zone plate boundary. In Kelemen, P.B.,
714 Matter, J.M., Teagle, D.A.H., Coggon, J.A., et al., Proceedings of the Oman Drilling
715 Project: College Station, TX (International Ocean Discovery Program).
716 https://doi.org/https://doi.org/10.14379/OmanDP.proc.2020
717
718 Ketcham, R. A., & Carlson, W. D. (2001). Acquisition, optimization and interpretation of X-ray
719 computed tomographic imagery: applications to the geosciences. *Computers &*
720 *Geosciences, 27*(4), 381-400.
721
722 Kyle, J. R., & Ketcham, R. A. (2015). Application of high resolution X-ray computed tomography
723 to mineral deposit origin, evaluation, and processing. *Ore Geology Reviews, 65*, 821-839.
724
725 Mavko, G., Mukerji, T., & Dvorkin, J. (2020). *The rock physics handbook*. Cambridge university
726 press.
727

McBeck, J., Cordonnier, B., Mair, K., & Renard, F. (2019). The evolving energy budget of experimental faults within continental crust: Insights from in situ dynamic X-ray microtomography. *Journal of Structural Geology, 123*, 42-53.

Mees, F., Swennen, R., Van Geet, M., & Jacobs, P. (2003). Applications of X-ray computed tomography in the geosciences. *Geological Society, London, Special Publications, 215*(1), 1-6.

Menzel, M. D., Urai, J. L., de Obeso, J. C., Kotowski, A., Manning, C. E., Kelemen, P. B., Kettermann, M., Jesus, A. P., Harigane, Y., & Team, t. O. D. P. P. S. (2020). Brittle Deformation of Carbonated Peridotite—Insights From Listvenites of the Samail Ophiolite (Oman Drilling Project Hole BT1B). *Journal of Geophysical Research: Solid Earth, 125*(10), e2020JB020199. https://doi.org/https://doi.org/10.1029/2020JB020199

Mibe, K., Fujii, T., & Yasuda, A. (1999). Control of the location of the volcanic front in island arcs by aqueous fluid connectivity in the mantle wedge. *Nature, 401*(6750), 259-262.

Nakajima, J., & Uchida, N. (2018). Repeated drainage from megathrusts during episodic slow slip. *Nature Geoscience*, 1.

Nakano, T., Nakashima, Y., Nakamura, K., & Ikeda, S. (2000). Observation and analysis of internal structure of rock using X-ray CT. *Journal of Geological Society of Japan, 106*, 363-378.

Newnham, R. E. (2005). *Properties of materials: anisotropy, symmetry, structure*. Oxford University Press on Demand.

O'Connell, R. J., & Budiansky, B. (1974). Seismic velocities in dry and saturated cracked solids. *Journal of Geophysical Research, 79*(35), 5412-5426.

Okazaki, K., & Hirth, G. (2016). Dehydration of lawsonite could directly trigger earthquakes in subducting oceanic crust. *Nature, 530*(7588), 81-84. https://doi.org/10.1038/nature16501

Okumura, S., Nakamura, M., Tsuchiyama, A., Nakano, T., & Uesugi, K. (2008). Evolution of bubble microstructure in sheared rhyolite: Formation of a channel-like bubble network. *Journal of Geophysical Research, 113*(B7). https://doi.org/10.1029/2007jb005362

764
765 Omori, S., Komabayashi, T., & Maruyama, S. (2004). Dehydration and earthquakes in the
766 subducting slab: empirical link in intermediate and deep seismic zones. *Physics of the*
767 *Earth and Planetary Interiors, 146*(1), 297-311.
768
769 Peacock, S. M., Christensen, N. I., Bostock, M. G., & Audet, P. (2011). High pore pressures and
770 porosity at 35 km depth in the Cascadia subduction zone. *Geology, 39*(5), 471-474.
771 https://doi.org/10.1130/g31649.1
772
773 Renard, F., Cordonnier, B., Dysthe, D. K., Boller, E., Tafforeau, P., & Rack, A. (2016). A
774 deformation rig for synchrotron microtomography studies of geomaterials under
775 conditions down to 10 km depth in the Earth. *Journal of synchrotron radiation, 23*(4),
776 1030-1034.
777
778 Streit, E., Kelemen, P., & Eiler, J. (2012). Coexisting serpentine and quartz from carbonate-bearing
779 serpentinized peridotite in the Samail Ophiolite, Oman. *Contributions to Mineralogy and*
780 *Petrology, 164*(5), 821-837.
781
782 Takazawa, E., Okayasu, T., & Satoh, K. (2003). Geochemistry and origin of the basal lherzolites
783 from the northern Oman ophiolite (northern Fizh block). *Geochemistry, Geophysics,*
784 *Geosystems, 4*(2).
785
786 Tsuchiyama, A., Uesugi, M., Matsushima, T., Michikami, T., Kadono, T., Nakamura, T., Uesugi,
787 K., Nakano, T., Sandford, S. A., & Noguchi, R. (2011). Three-dimensional structure of
788 Hayabusa samples: origin and evolution of Itokawa regolith. *Science, 333*(6046), 1125-
789 1128.
790
791 Tsuji, Y., Nakajima, J., & Hasegawa, A. (2008). Tomographic evidence for hydrated oceanic crust
792 of the Pacific slab beneath northeastern Japan: Implications for water transportation in
793 subduction zones. *Geophysical Research Letters, 35*(14).
794 https://doi.org/10.1029/2008gl034461
795
796 Underwood, M. B., Saito, S., Kubo, Y., & the Expedition 322 Scientists. (2010). Expedition 322
797 summary In Saito, S., Underwood, M.B., Kubo, Y., and the Expedition 322 Scientists, Proc.
798 IODP, 322: Tokyo (Integrated Ocean Drilling Program Management International, Inc.). .
799 *Proc. IODP, 322*. https://doi.org/doi:10.2204/iodp.proc.322.101.2010

Yao, C., Wu, Z., Zou, F., & Sun, W. (2018). Thermodynamic and Elastic Properties of Magnesite at Mantle Conditions: First - Principles Calculations. *Geochemistry, Geophysics, Geosystems, 19*(8), 2719-2731.